Proceedings of the 28th IEEE
EMBS Annual International Conference
New York City, USA, Aug 30-Sept 3, 2006

Tailoring magnetic field gradient design to magnet cryostat geometry

A. Trakic, F. Liu, H. S. Lopez, H. Wang and S. Crozier

Abstract – **Eddy currents induced within a Magnetic Resonance Imaging (MRI) cryostat bore during pulsing of gradient coils can be applied constructively together with the gradient currents that generate them, to obtain good quality gradient uniformities within a specified imaging volume over time. This can be achieved by simultaneously optimizing the spatial distribution and temporal pre-emphasis of the gradient coil current, to account for the spatial and temporal variation of the secondary magnetic fields due to the induced eddy currents. This method allows the tailored design of gradient coil/magnet configurations and consequent engineering trade-offs. To compute the transient eddy currents within a realistic cryostat vessel, a low-frequency Finite-Difference Time-Domain (FDTD) method using Total-Field Scattered-Field (TFSF) scheme has been performed and validated.**

I. INTRODUCTION

When pulsing magnetic field gradients during MRI spatial encoding, multi-exponentially decaying eddy currents are always induced within the conducting system components [1-2]. These secondary magnetic fields are known to cause spatial and temporal degradation in the gradient uniformity within the imaging volume, which often result in undesired misregistration and intensity-phase variations in both images and spectra. With the recent push of MRI towards high signal to noise ratios (SNR) and improved image resolution, tremendous efforts have been made to prevent and minimize the eddy current fields. For instance, active screening is often engaged to minimize leakage fields and hence spatially and temporally complex residual eddy current (REC) induced in the cryostat vessel [3-5]. Unfortunately, the use of active shielding layer(s) occupies vital MRI space, increases system cost and reduces gradient efficiency. Besides, REC is never completely removed through active screening and B_0-shift compensation and pre-emphasis of gradient coil currents are also required for optimal results [6-7]. Gradient coils designs normally employ active shielding to reduce leakage fields and consequently REC magnitudes in the cryostat vessel. Typically, little attention is given to the actual spatial variation and temporal behaviour of induced currents triggered by the particular gradient coil geometry and switching characteristics. The B_0-shift compensation and gradient current pre-emphasis are usually adjusted experimentally.

According to a number of studies presented in recent years [3-7], residual eddy current appear inevitable. In this work we explore the possibilities of including predicted eddy currents in the design process of the gradient coil.

Given any kind of gradient coil and fixed, realistic cryostat vessel geometry, the spatial distribution and temporal pre-emphasis of the gradient coil current are simultaneously tailored to accommodate for the presence of transient eddy currents induced within the cryostat bore and other conducting system components. It is shown that with a suitable temporal pre-emphasis and the optimized spatial current distribution, the multi-exponentially decaying eddy currents can be accurately predicted, controlled and constructively used to assist in shaping very uniform and temporally stable gradient fields.

I. METHODOLOGY

A. The TFSF-FDTD formulation

In this work, we exemplify the method with the design of a z-gradient coil in the presence of a multi-layer cryostat. The central-difference method is applied to the Maxwell's curl equations in two-dimensional (2D) axial symmetric cylindrical coordinates to obtain a set of general FDTD update formulations for the fields inside the conductor (here: cryostat vessel) and surrounding medium [8]:

$$H_r\big|_{i,k+1/2}^{n+1/2} = H_r\big|_{i,k+1/2}^{n} + \frac{\Delta t}{\mu}\left(\frac{E_\varphi\big|_{i,k+1}^{n} - E_\varphi\big|_{i,k}^{n}}{\Delta z}\right) \tag{1}$$

$$H_z\big|_{i+1/2,k}^{n+1/2} = H_z\big|_{i+1/2,k}^{n} + \frac{\Delta t}{\mu_{i+1/2}}\left(\frac{r_{i+1}E_\varphi\big|_{i+1,k}^{n} - r_i E_\varphi\big|_{i,k}^{n}}{\Delta r}\right) \tag{2}$$

$$E_\varphi\big|_{i,k}^{n+1} = \left(\frac{2\varepsilon_0 - \sigma\Delta t}{2\varepsilon_0 + \sigma\Delta t}\right)E_\varphi\big|_{i,k}^{n} + \left(\frac{2\Delta t}{2\varepsilon_0 + \sigma\Delta t}\right)\begin{pmatrix}\dfrac{H_r\big|_{i,k+1/2}^{n+1/2} - H_r\big|_{i,k-1/2}^{n+1/2}}{\Delta z} \\ -\dfrac{H_z\big|_{i+1/2,k}^{n+1/2} - H_z\big|_{i-1/2,k}^{n+1/2}}{\Delta r}\end{pmatrix} \tag{3}$$

where Δr and Δz are radial and axial cell size, respectively. The relative permeability $\mu_r(r,z)$, relative permittivity $\varepsilon_r(r,z)$ and material conductivity $\sigma(r,z)$ are defined at the center of the Yee cell. The TFSF method [8] is then engaged to minimize the computational burden associated with the redundant evaluation of the electromagnetic (EM) fields within the air domain. With the TFSF formulation in place, only the conductor and a small region of air neighbouring the conductor need to be discretized. The gradient coil source field is then propagated analytically to the TFSF boundaries surrounding the cryostat (shown in figure 1) using elliptic integrals for radial and axial magnetic and azimuthal electric field components [9]. The transient TFSF boundary conditions can be written:

BOTTOM INTERFACE:

$$H_r\big|_{i,k0-1/2}^{n+1/2} = H_r\big|_{i,k0-1/2}^{n+1/2} - \Xi\left(\frac{\Delta t\overline{E}_\varphi\big|_{i,k0}}{\Delta z\mu}\right) \qquad E_\phi\big|_{i,k0}^{n} = E_\phi\big|_{i,k0}^{n} - \Xi\left(\frac{2\Delta t\overline{H}_r\big|_{i,k0-1/2}}{2\varepsilon_0\Delta z + \sigma\Delta t\Delta z}\right) \tag{4}$$

TOP INTERFACE:

$$H_r\big|_{i,k1+1/2}^{n+1/2} = H_r\big|_{i,k1+1/2}^{n+1/2} + \Xi\left(\frac{\Delta t\overline{E}_\varphi\big|_{i,k1}}{\Delta z\mu}\right) \qquad E_\phi\big|_{i,k1}^{n} = E_\phi\big|_{i,k1}^{n} + \Xi\left(\frac{2\Delta t\overline{H}_r\big|_{i,k1+1/2}}{2\varepsilon_0\Delta z + \sigma\Delta t\Delta z}\right) \tag{5}$$

LEFT INTERFACE:

$$H_z\big|_{i0-1/2,k}^{n+1/2} = H_z\big|_{i0-1/2,k}^{n+1/2} + \Xi\left(\frac{r_{i+1}\Delta t\overline{E}_\varphi\big|_{i0,k}}{r_{i+1/2}\Delta r\mu}\right) \qquad E_\phi\big|_{i0,k}^{n} = E_\phi\big|_{i0,k}^{n} + \Xi\left(\frac{2\Delta t\overline{H}_r\big|_{i0-1/2,k}}{2\varepsilon_0\Delta z + \sigma\Delta t\Delta r}\right) \tag{6}$$

RIGHT INTERFACE:

$$H_z\big|_{i1+1/2,k}^{n+1/2} = H_z\big|_{i1+1/2,k}^{n+1/2} + \Xi\left(\frac{r_i\Delta t\overline{E}_\varphi\big|_{i1,k}}{r_{i+1/2}\Delta r\mu}\right) \qquad E_\phi\big|_{i1,k}^{n} = E_\phi\big|_{i1,k}^{n} - \Xi\left(\frac{2\Delta t\overline{H}_r\big|_{i1,k-1/2}}{2\varepsilon_0\Delta z + \sigma\Delta t\Delta r}\right) \tag{7}$$

Where the incident fields are given by $\overline{H}_r$, $\overline{H}_z$ and $\overline{E}_\phi$.

The TFSF boundary is assumed to be a rectangular box with the following discrete limits:
$i = \{i \in N \mid i_0 \le i < i_1\} \wedge k = \{k \in N \mid k_0 \le k < k_1\}$.

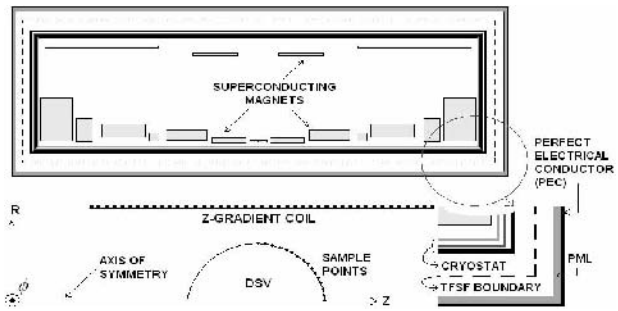

Figure 1 – MRI system setup showing the z-gradient coil and the TFSF boundary enclosing the cryostat vessel. PEC encloses the TFSF-FDTD computational domain.

The operator Ξ represents the temporal excitation used in driving the gradient coil. For instance, in MRI, the Echo Planar Imaging sequence (EPI) employs low frequency trapezoidal current pulses that drive the gradients to facilitate the generation of high-resolution images. The TFSF-FDTD domain is terminated in a cylindrical split-version Perfectly Matched Layer (PML) absorbing boundary condition [8] where only the azimuthal and axial EM-field components need to be considered.

B. Adaptation of TFSF-FDTD to low frequencies

FDTD is a popular scheme for the solution of high frequency problems, due to its simplicity and efficiency in wave models. At low frequencies, however, Maxwell's equations lose their symmetry, as the conducting current is many orders of magnitude larger than the displacement current. Nevertheless, the standard FDTD scheme can be adapted to low frequencies by appropriate linear scaling of certain physical system parameters [10]. One way to achieve the adaptation is to scale up the permittivity of free space ε_0 and to leave the permeability μ_0 unchanged. The downscaled speed of light constant c_α is then written:

$$c_\alpha = \frac{1}{\sqrt{\mu_0(\alpha\varepsilon_0)}} = \frac{1}{\sqrt{\mu_0\varepsilon_\alpha}} \tag{9}$$

where α is a dimensionless scaling factor, μ_0 is the permeability of free space $[4\pi\cdot10^{-7}WbA^{-1}m^{-1}]$, ε_0 is the permittivity of free space $[8.8542\cdot10^{-12}C^2N^{-1}m^{-2}]$ and ε_α is the scaled free space permittivity.

C. Eddy current and magnetic field computation

The TFSF-FDTD formulation allows direct and efficient numerical computation of eddy currents induced within the conducting volume (cryostat vessel) during pulsing of magnetic field gradients. According to Amperes Law, the eddy currents will generate a secondary magnetic field, which by its nature will oppose the incident magnetic field generated by the gradient coil. Using the superposition theorem, the secondary transient magnetic field in the imaging volume of the gradient coil can be obtained by numerical integration provided the eddy current electric field in the conducting region is known *a priori*. Firstly, the eddy current within every Yee cell of the conducting region $I_{eddy} = \sigma E_{eddy}\Delta r\Delta z$ is computed, followed by numerical integration of the induced eddy current to obtain the corresponding secondary magnetic field within the diameter spherical volume (DSV).

D. Verification of the TFSF-FDTD scheme

The cylindrical TFSF-FDTD formulation has been validated against a numerical model using the Finite Element software package FEMLAB©. First, an unshielded 20-turn symmetric z-gradient is designed to have a diameter of 710mm with axial coil coordinates detailed in Table I. The gradient coil generates a DSV (here: < 5% peak-to-peak (pp) gradient uniformity error) with radial and axial diameters of 0.45m.

TABLE I

AXIAL COIL COORDINATES [mm]									
139	322	382	449	460	522	527	539	581	590

A trapezoidal current (maximum amplitude $1\ A/m^2$) at a frequency and rise time of $1\ kHz$ and $100\ \mu s$, respectively, has been used to excite the coil. The gradient coil is embedded in a realistic cylindrical cryostat vessel consisting of stainless steel and two aluminium radiation shield layers. Table II lists the physical properties of the cryostat vessel walls. The total length of the cryostat vessel was assumed to be 1.4m.

TABLE II

#	Material	Conductivity [MS/m]	Thickness [mm]	Inner Radius [m]
1	Stainless Steel	~ 1.05 @ 300K	5	0.4505
2	Aluminium	~ 100 @ 80K	3	0.4655
3	Aluminium	~ 500 @ 4.3K	6	0.4785

With a radial and axial Yee cell size of 0.25mm and 7mm, respectively, the cryostat vessel was suitably discretized to capture the spatial exponential decay (skin effect) of propagating waves as they penetrate the conducting walls.

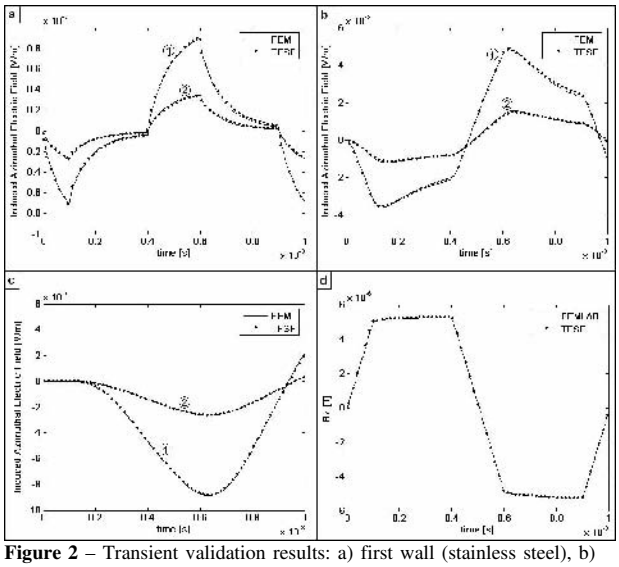

Figure 2 – Transient validation results: a) first wall (stainless steel), b) second wall (aluminium) and c) third wall (aluminium), where waveform 1 and waveform 2 are spatial points taken at the inner surface 0.21m and 0.07m axially from the center of axis of symmetry, respectively. Subplot d) represents the secondary axial magnetic flux density due to the whole cryostat vessel at R=0; Z=0.225m.

With the scaling factor of $\alpha = 9\cdot10^{10}$, it took around 8 seconds to obtain the result for one period of the trapezoidal sequence. An identical model has been set-up in FEMLAB with 31560 degrees of freedom. Figure 2 compares the transient, azimuthal eddy current electric fields at different locations within the cryostat vessel between the TFSF-FDTD and FEMLAB simulations. The validation results agree well. The aforementioned system

parameters will be assumed same throughout this study, if not stated otherwise.

E. General gradient design including eddy currents

The methodology of this work considers the transient eddy currents induced in an example cryostat (Table II) and the corresponding effects in the DSV region during the design of the gradient coil. Ideally, both the induced eddy and gradient coil currents are accountable for the target field uniformity in the imaging volume. To achieve the desired gradient homogeneity over time, both the spatial distribution and temporal pre-emphasis of the gradient coil current are taken into account for the spatial and temporal presence of the eddy current fields. It is essential that the spatial distribution and temporal overshoot of the gradient coil current be coupled during the optimisation process in order to control and make best use of induced eddy currents.

In one approach, the gradient coil is first designed without the consideration of eddy currents using on of the many design schemes available [11]. During this stage, it is possible to include any of the conventional constraints and objectives. The stand-alone gradient coil is then theoretically placed within a model cryostat vessel, such as the one outlined in Table II, and the desired switching sequence is applied. At several time points, the primary and secondary magnet field is computed on the DSV periphery and the desired objective function is derived. Then using an optimisation scheme (here: Levenberg-Marquardt [LM]) the coil current distribution (or discrete coil wires) is perturbed. The desired temporal gradient uniformity is targeted to be same as the switching sequence – i.e. analogous to the gradient coil current excitation under absence of the cryostat vessel.

III. RESULTS AND DISCUSSION

Although the outlined methodology can be applied to any known gradient coil type and geometry, for the purposes of a demonstration of the proposed technique, only actively shielded and unshielded symmetric z-gradient coils are considered *herein*.

A. Single Layer Z-Gradient Coil

A shorter version of the z-gradient coil from Table I, with an overall length of 1m, has been implemented. It has been assumed that the coil is made of circular copper wires with 3mm in diameter. The optimisation procedure is terminated when the maximum deviation of less than 5%pp from the desired gradient over time is achieved, which in this case was after around 28 minutes of CPU time and 6.3 MB of memory usage on two XEON 3.6 GHz processors with 4 GB of memory each. Figure 3 illustrates the maximum deviation of the gradient uniformity from the target gradient over time and the optimized solution achieved through suitable current pre-emphasis and appropriate variation in axial coil positions. The scaled version of the required pre-emphasized current excitation is also illustrated in the same plot. The same optimisation procedure was applied to the longer z-gradient coil from Table I with similar CPU time and memory requirements.

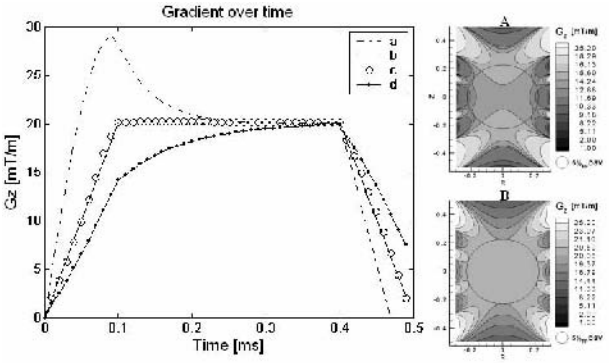

Figure 3 – *Left*: Gradient field versus time at 500A transport current: a) sketch of scaled pre-emphasised current excitation, b) closest desired gradient uniformity over time, c) optimised gradient uniformity where eddy currents are taken into account and d) maximum spatial gradient uniformity degradation over time due to eddy currents (non-optimised gradient case). *Right:* Gradient uniformity snapshots at 500A transport current at 0.1ms of trapezoidal excitation: A) due to non-optimised gradient coil and induced transient eddy currents and B) due to spatially and temporally optimised gradient coil and eddy currents. The gradient uniformity in B) is preserved during the whole excitation.

Table III lists the axial coordinates of the non-optimized and optimized gradient coil, indicating change in axial positions required to accommodate for the presence of eddy currents.

TABLE III

COIL	AXIAL COIL COORDINATES [mm]									
STANDARD	140	340	345	355	425	455	463	480	485	500
OPTIMISED	140	335	340	353	425	494	463	480	485	500
CHANGE	0	-5	-5	-2	0	+39	0	0	0	0

Through simultaneous application of current pre-emphasis (figure 4) and optimized axial coil positions (Table III), high spatial gradient uniformity (with < 5% pp gradient uniformity error) over time can be achieved.

B. Actively Shielded Z-Gradient Coil

In this part of the study an actively shielded stand-alone symmetric z-gradient coil has been implemented. The gradient coil optimisation aims were to minimize the leakage fields at the first eddy current source, maximize the gradient efficiency and obtain at most 5%pp gradient uniformity in a 500 x 560mm working volume. The inner and outer coil diameters were fixed at 700mm and 800mm respectively. We have then situated the actively shielded gradient coil inside the same cryostat vessel (Table II) and tailored the gradient current overshoot and optimised axial coil positions in both the primary and secondary gradient layer to account for eddy current fields. The leakage fields were also minimised during the same optimisation process. Table IV lists the axial coordinates for the non-optimised and optimised gradient coils, indicating change in axial positions required in the presence of eddy currents. With active shielding, the magnitude of the eddy currents in the cryostat is reduced while the coil efficiency has been minimized. Around 4.0% pre-emphasis overshoot was required and yet variation in axial coil positions remains advantageous to produce the best coil performance, as illustrated in figure 4.

TABLE IV

1st layer	AXIAL COIL COORDINATES [mm]														
STANDARD	98	196	221	282	362	395	411	419	452	455	458	461	464	467	480
OPTIMISED	95	193	223	286	362	392	410	415	445	449	455	459	464	472	479
CHANGE	-3	-3	+2	+4	0	-3	-1	-4	-7	-6	-3	-2	0	+5	-1
2nd layer															
STANDARD	115	198	269	341	380	416	434	463	482	526					
OPTIMISED	112	200	278	339	380	413	433	467	483	528					
CHANGE	-3	+2	+9	-2	0	-3	-1	+4	+1	+2					

The proposed method provides distinct advantages in the systems engineering of gradient coil/magnet pairs as the cryostat and gradient set can be designed together in terms of eddy current induction and field profiles. This also allows the rapid design prototyping of cryostats of various shapes and properties. Although z-gradient coils were considered in this work, the methodology can be easily extended to transverse gradient coils, where the current distribution on the cylindrical surface is optimised both spatially and temporally to account for the presence of eddy currents induced in the fixed cryostat vessel.

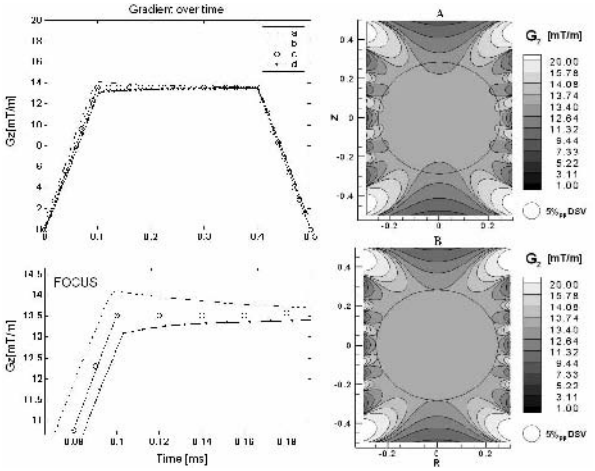

Figure 4 – *Left*: The gradient field versus time for actively shielded coil at 500A transport current (analogous to Figure 3 (left)). Shown below is the focused plot at around 0.1ms of trapezoidal excitation illustrating that the optimised gradient uniformity is following the closest desired gradient (e.g. trapezoidal profile). *Right:* The gradient uniformity snapshots at 500A transport current at 0.1ms of trapezoidal excitation: A) due to the non-optimised gradient coil and induced transient eddy currents and B) due to spatially and temporally optimised gradient coil and eddy currents.

The unshielded gradient coil (Table III) is around 1.46 times more efficient than the shielded gradient coil (Table IV) under the same transport current conditions. Obviously displacing the active shield further away from the primary coil would improve the gradient efficiency. However, the unshielded coil requires much more voltage overdrive (figure 3) than the actively shielded gradient and hence imposes more burdens on the amplifier system. Figure 5 illustrates the effects of pre-emphasis and perturbed current distribution on the spatial and temporal characteristics of the induced eddy currents. The largest eddy currents are induced in the second cryostat wall, as this is the first electromagnetic shield with reasonably high material conductivity. The electromagnetic energy diffuses slowly through this second layer and, as expected, the eddy current excitation in the third wall is considerably delayed in time. In addition, one can observe different decay terms within the cryostat vessel due to diverse material properties and unique wall geometries within the cryostat vessel.

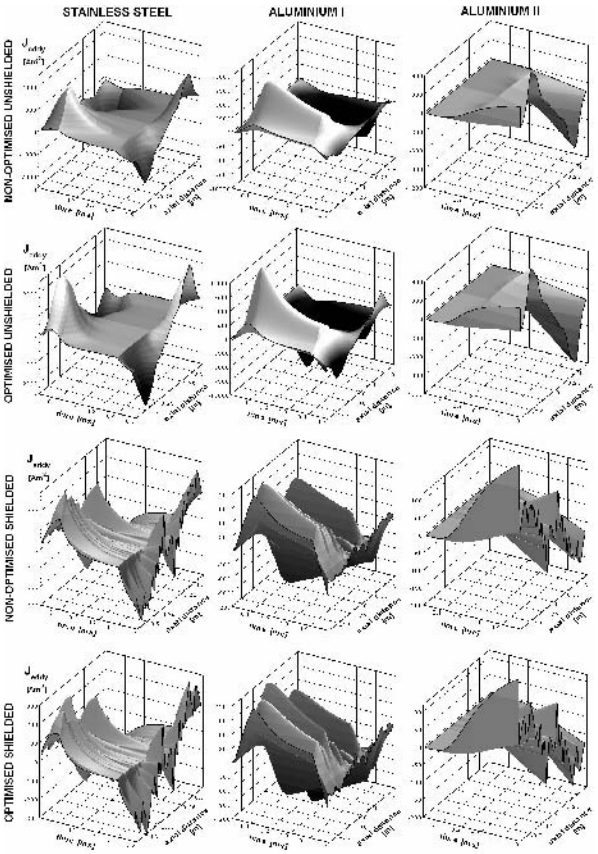

Figure 5 – Eddy current density along the z-axis versus time at the inner surface of the stainless steel, aluminium I and aluminium II cryostat walls for the non-optimised and optimised unshielded (TableIII) and actively shielded symmetric z-gradient coils at 1A transport current.

IV. CONCLUSION

Gradient coils can be implemented to produce very uniform gradient fields over time by taking into account the transient eddy currents induced in the cryostat vessel and other conducting MRI system components. The compensation can be achieved through coupled optimisation of spatial distribution and pre-emphasis of the gradient coil current that accounts for the presence of eddy current field and should be preferably applied during the design process of the gradient coil. In future work, we intend to study the implication of different imaging modalities, rise-times and gradient coil/cryostat vessel geometries and intrinsic properties on the target gradient uniformity, using the new method.

REFERENCES

[1] E. Badea *et. al*., *IEEE Trans. Magn.*, 33(2): 1330-1333, 1997.
[2] G. Ries, *IEEE Trans. Magn.*, 24(1):516-519, 1988
[3] S. Shvartsman *et. al*., *Conc. Magn. Reson. B*, 26B (1) 1-15, 2005
[4] P. Mansfield *et. al.* , *J. Phys.E: Sci. Inst.*, 19: 540:545, 1988
[5] S. Crozier et. al. , *Magn. Reson. Imag.*, 13(4): 615-620, 1995
[6] H. M . Gach *et. al*., *J*. Magn. Reson. Med., 40: 427-431, 1998
[7] S. Crozier *et. al*., *J. Magn. Reson. 97*, 661-665, 1992.
[8] A. Taflove, "Computational Electromagnetics – The Finite-Difference Time-Domain Method ", (London: Artech) 1995
[9] M. Abramowitz and I. A. Stegun, "Handbook of mathematical functions", London, Dover, 1965
[10] R. Holland, *IEEE Trans. Anten. Prop*, 43(7), 653-659, 1995
[11] R. Turner, *Magn. Reson. Imag.*, 11: 903-920, 1993.